This is the Pre-Published Version.

Z. Zhang, P. Ding, S. Wang, X. Huang (2023) *Smouldering-to-Flaming Transition on Wood Induced by Glowing Char Cracks and Cross Wind*, **Fuel**, 352, 129091. https://doi.org/10.1016/j.fuel.2023.129091

Smouldering-to-Flaming Transition on Wood Induced by Glowing Char Cracks and Cross Wind

Ziyang Zhang [a, #], Pengfei Ding [b, #],Supan Wang [a, *], Xinyan Huang [c, *]

[a] *College of Safety Science and Engineering, Nanjing Tech University, Nanjing, China*

[b] *Shanghai Fire Research Institute of MEM, Shanghai 200032, China*

[c] *Research Centre for Fire Safety Engineering, Department of Building Environment and Energy Engineering, The Hong Kong Polytechnic University, Kowloon, Hong Kong*

[#] Ziyang Zhang and Pengfei Ding, as the co-first authors, contributed equally to the paper

*Corresponding to wangsp@njtech.edu.cn (S. Wang), xy.huang@polyu.edu.hk (X. Huang)

Abstract:

The shrinkage, deformation and cracking of the wood affect their smouldering and flaming dynamics, but the scientific understanding is still limited. We study the burning behaviours of disc wood samples with a diameter of 60 mm and thicknesses of 5-40 mm under external airflows up to 6 m/s. Results show that the smouldering-to-flaming (StF) transition can be observed at about 830 °C under external airflow, which is caused by the interactions between smouldering-induced crack and environmental airflow. The fully penetrated vertical char crack or pre-perforated hole promotes the StF transition because of (1) enhanced radiation between the two smouldering surfaces and (2) greater air supply under the chimney effect. As the wind velocity increases, both the smouldering surface temperature and crack size increase, so the transition to flaming becomes faster. For a larger wood thickness, a larger airflow is required to generate the crack and cause a StF transition. A numerical model is proposed to investigate the volatile convection and flaming ignition. Numerical analysis reproduces the StF transition, as an autoignition of a pyrolysate-oxygen mixture promoted by hot smouldering surfaces. The numerical model further reveals the effects of smouldering temperature and cross wind on the StF transition. This work deepens the understanding of the StF transition dynamics and provides insights into the wildfire ignition dynamics and fire hazards of timber structures.

Keywords: *Timber fire; Wildfire; Smouldering simulation; Oxygen supply; Cracking; Wind effect*

Graphic Abstract

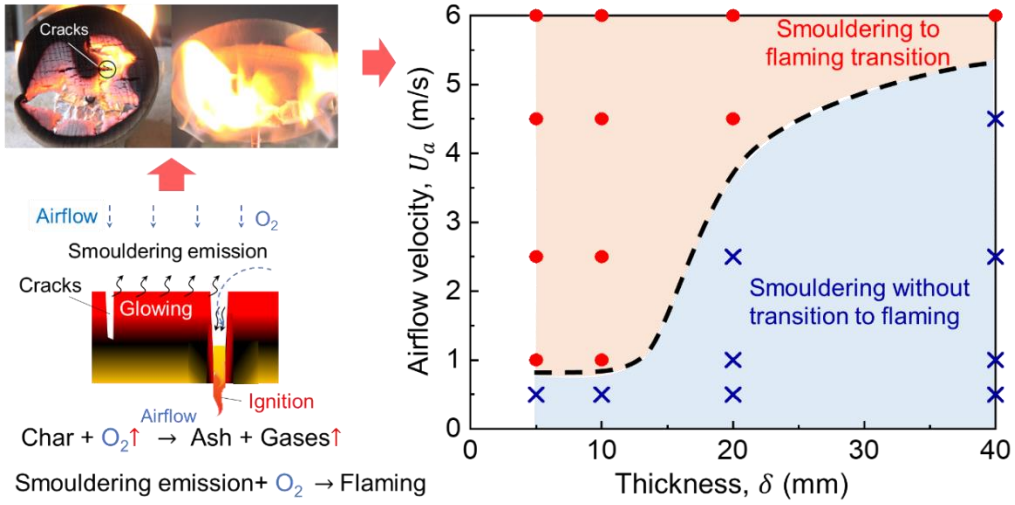

1. Introduction

Wood is one of the longest-standing construction, and current sustainable construction materials for high-rise timber buildings (Fig. 1a), because of its cost-effectiveness, high strength-to-weight ratio, and environmental-friendly to achieve carbon neutrality globally [1,2]. Wood is also the dominant fuel in wildland fires. However, the fire risk of wood is still a primary safety concern, due to its combustible nature [3] and large fuel loads [4,5], i.e., fire accidents of the medieval Notre Dame Cathedral in Paris (Fig. 1b) and large-scale wildfires worldwide [6]. The burning of wood generates a porous char layer and causes shrinkage, deformation and cracking behaviours. In turn, these wood structural variations also change smouldering and flaming dynamics. However, the reserve effect of the glowing char cracks on the wood combustion is still not fully understood.

When the wood is heated, the material decomposes to release flammable gases, and leaves behind a porous char layer (Fig.1c). The char layer has a lower permeability to oxygen diffusion, and may act as an important heat barrier between the combustion and virgin material, even resulting in the self-extinction of the wood [4]. It has been widely observed that a single flat, thermally thick slab of wood is difficult to smoulder unless the smoulder-derived heat is supplemented by an external radiant flux. But a stable smouldering on solid wood has been conducted by a U-shaped channel sample [7], which is self-sustained by radiative interactions among elements of the surface. Herein, the shrinkage and deformation of the porous char layer are always accompanied by the form of the char fissures, which increase the heat transfer of radiation, and provide a shortcut path to the permeability of the oxygen diffusion. The current research focuses on the “char shrinkage and cracking” behaviour during pyrolysis in different ambient pressures [8,9], and the deformation behaviours of disc wood slices in the interactions between smouldering combustion and thermo-mechanical stress [10]. It is difficult to judge the glowing char cracks’ effect on the heat transfer and combustion of solid wood.

Fig. 1. (a) The 18-storey timber Brock Commons in Canada (Credit: Michael Elkan), (b) fire accidents of the medieval Notre-Dame Cathedral in Paris (Photo courtesy Wiki Commons), (c) crack of the wood in the fire (Credit: Ivan-balvan), and (d) smouldering and flaming combustion of the wood (Credit: Depositphotos).

Almost all cellulose fuels can sustain both forms of flaming and smouldering combustion [11,12], the smouldering process can lead to flaming combustion normally in powdery or porous solid fuels [13–15], which mainly contain polyurethane foams [16,17], cotton [18], or discrete cellulose powders like particle board, sawdust and shredded wood [14]. Smouldering-to-flaming (StF) transition is a complex process in which the smoulder reaction provides the heat to pyrolyze the virgin fuel, or acts as a pilot to ignite the flammable gaseous mixture, involving the transition from "heterogeneous reactions" to "homogeneous gas phase reactions". The current research reported the flaming and smouldering behaviours of wood [3], and Lin *et al.* also reported the coexistence of smouldering and flaming at the crack for a near-limit blue flame [19]. It is difficult to judge whether materials with a lower-porosity medium like solid wood, can support a StF transition.

The buoyancy-induced airflow of flame will be enhanced by increased curvature of the crack surface [20] and temperature of glowing phenomena at char fissures. Smouldering spread may transition into a sustained flame spread, especially under the assistance of wind [21]. Ohlemiller found that the forward horizontal smouldering responded strongly to the airflow, and the critical airflow velocity that yielded transition to flaming at about 0.5~2 m/s depended on fuel chemistry [22]. Yang concluded that the StF transition ultimately occurred at 2-3 cm above the leading edge of the smouldering front on the top surface under a windy environment [23]. The above research focused on cellulosic insulation with < 100 kg/m^3 density, while to the best of the authors' knowledge, the StF transition of real solid wood with various ambient wind speeds has not been systematically studied yet, posing a knowledge gap.

In the present work, well-controlled experiments were conducted to investigate the burning behaviours of small-scale disc wood samples. The StF transition and the characteristic temperature of the wood sample were determined. The limit of the StF transition was quantified as the function of sample thicknesses and wind speeds. The fully penetrated vertical char crack or pre-perforated hole was used to verify the smouldering vertical char cracks (like a chimney channel) effect on the StF transition.

This research will contribute to the understanding of the StF transition dynamics of solid wood.

2. Experimental method

2.1. Setup and controlling parameters

Solid beech wood slices were chosen in this experiment and cut perpendicular to the grains. This wood is representative biomass species in the southern forest of China, and it is widely used in building constructions and furniture. All samples were first oven-dried at 80 °C for 8 h, and then stored in the temperature and humidity chamber. Before the test, the sample was measured to have a density of 653.8 ± 15.8 kg/m^3 and moisture content of 9 ± 1% at an ambient temperature of 15 °C, and relative humidity of 35 ± 2%.

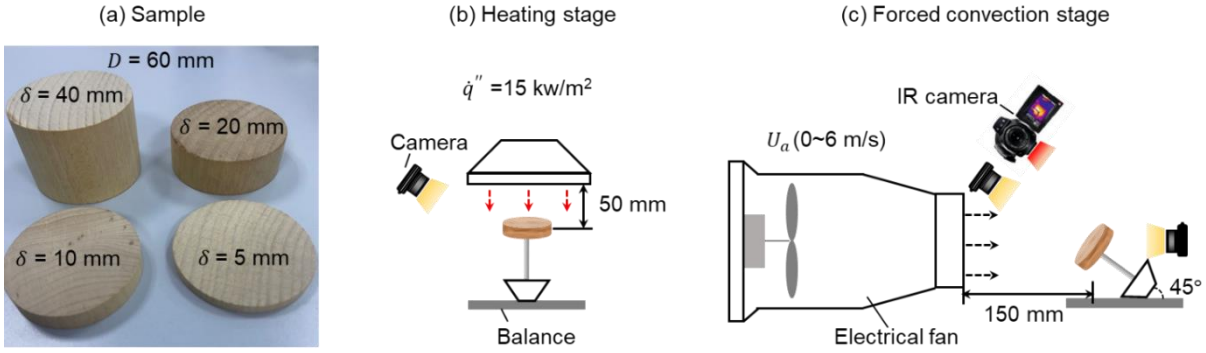

Fig. 2. Schematic diagram of the designed experimental setup.

Based on the common thicknesses of wooden furniture (10-45 mm), engineered timber (12-40 mm), and timber structures (> 40 mm), four 60 mm-diameter (D) samples with different thicknesses (δ) of 5, 10, 20 and 40 mm were tested in Fig. 2a. Their initial mass ranges from 8.9 ± 0.4 g to 74.1 ± 2.1 g, shown more in Tab. 1. The centre point of the bottom of the wood slice was glued with a 0.2-mm-diameter aluminium rod stick, which acted as a sample holder [10] in Fig. 2b-c. Afterwards, it was placed for 5 h to stabilize the glued connection between the stick and the sample.

Table 1 Parameters of the wood samples and airflow velocity in the experiment.

Thickness (δ, mm)	Diameter (D, mm)	Weight (g)	Airflow velocity (U_a, m/s)
5	60	8.9 ± 0.4	0, 0.5, 1, 2.5, 4.5 and 6
10		18.7 ± 0.7	
20		37.6 ± 1.2	
40		74.1 ± 2.1	

Figure 2 shows the schematic diagram of the experimental setup, which consists of a blower, a cone-shaped heater, a sample holder, and a data collection system. The blower was used to generate a uniform environmental airflow at 150 mm from the outlet. In this system, one SF4-4 Type axial flow fan controlled by powder transducers (range: 0–50 Hz, resolution: 0.1 Hz) and a 2 m-long fairing [24],

were used to mimic the velocity of buoyancy-induced airflow in flame and provide the desired airflow. The airflow velocity (U_a) was calibrated with the frequency of the transducers, and 0 to 6 m/s cross wind was used, corresponding to the natural wind of magnitude 1-4. The cone-shaped heater was placed 50 mm above the sample, which provided uniform irradiation up to 60 kW/m^2 on the top surface. The irradiation of 15 kW/m^2 was applied, considering this value is strong enough to initiate a smouldering ignition of beech wood [11]. The evolution of mass loss ($\dot{m}''$) for samples has been tracked in the experiments, but the effect of airflow on mass loss is significantly larger than that of smouldering and flaming burning, which won't be reported in this work.

2.2. Test procedures

Before the test, the level of irradiation and airflow was adjusted by changing the heating power and the frequency of the transducers, to be calibrated by a radiometer (GTW-12.7-100) and anemometer (Smart senor AR866A), respectively. The experiment can be separated into heating and force convection stages. Once the irradiation became steady-state, the wood was quickly exposed to the irradiation, until the glowing ignition emerged on the edge of the crack, as shown in Fig. 2b. Then, the sample was quickly 45° exposed to the outlet of the blower by adjusting the contact between the sample holder and balance, as shown in Fig. 2c. Here, the airflow started once the shield of the blower was removed, and the evolution of smouldering propagation could be observed at the given airflow.

For the wood thickness, the test was started with the thinnest thickness (δ = 5 mm). If the smouldering successfully transitioned to the flaming, the sample thickness was then increased gradually until the smouldering front could no longer transition. Then, the maximum wood thickness for the StF transition (δ^*) could be determined. Afterwards, conditions of airflow velocities were changed to explore the variation in the critical thickness.

To record the StF phenomena, the heating stage was recorded with on video camera from the 45° top view, and the force convection stage was recorded with two video cameras (Sony FDR-AX60 at 50 fps) to capture both top and bottom surfaces from the 45° top and side views, respectively. To quantify the temperature distribution, the IR camera was kept perpendicular to the top surface of the sample. The mass loss, temperature distribution, and surface phenomena could be recorded throughout the experiment. The mass evolution of the wood sample was measured by the electric balance (Mettler-Toledo XE10002S, resolution: 0.01 g). For each scenario, tests were repeated at least three times, and good experimental repeatability was found.

3. Results and discussion

3.1. Phenomena of StF transition

During the heating process, the sample went through the release of visible smoke, strong pyrolysis (or charring), and char oxidation. Moreover, the raw sample was transformed into a more porous char, and the char may shrink and crack, even forming char fissures. These behaviours of the heating stage

are the same as the past findings [10,11,25], and not presented here. When the glowing combustion at the edge of the crack occurred, the sample was exposed to the forced convective environment (time t = 0 s in Fig. 3).

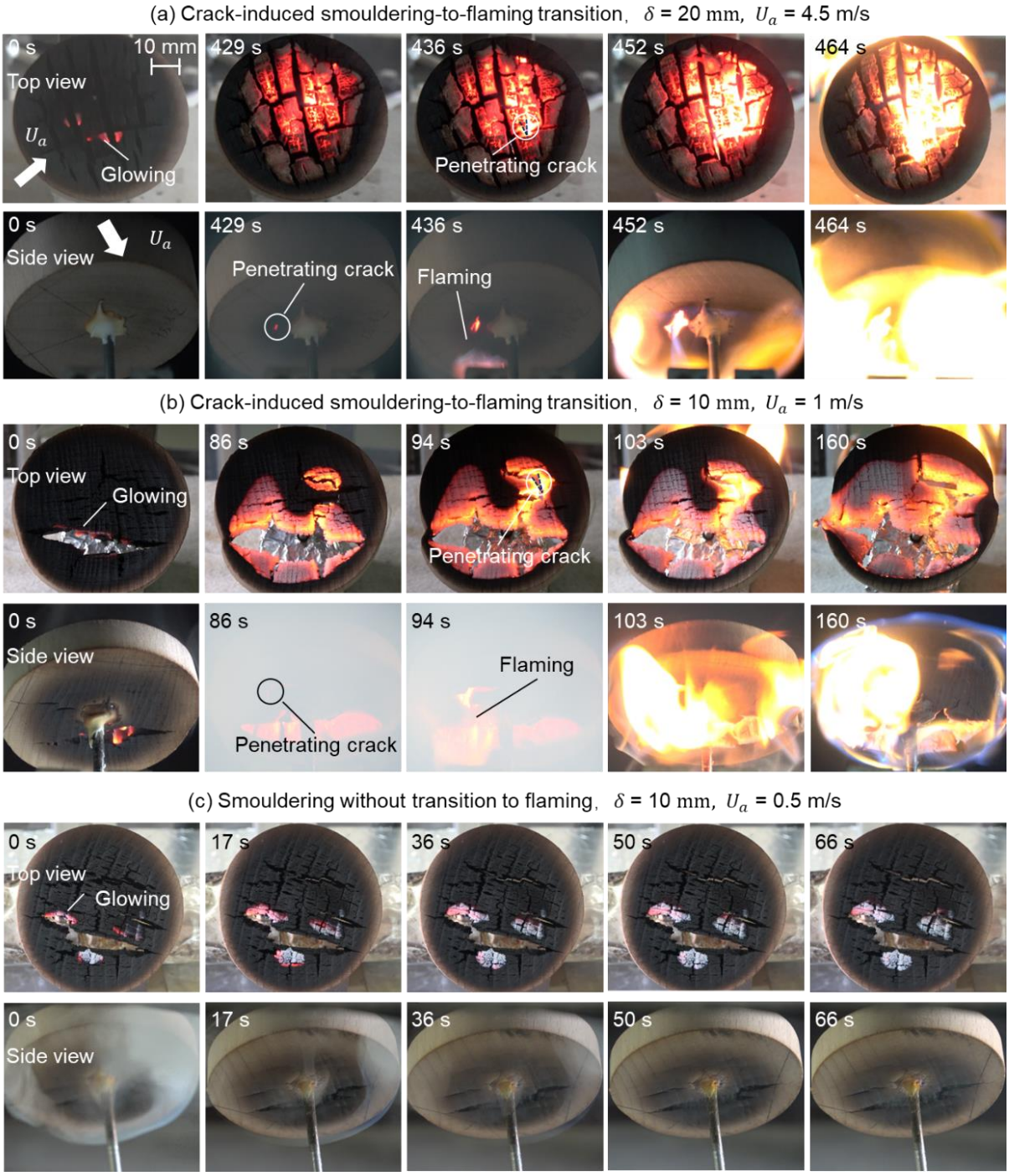

Fig. 3. Snapshots of the possible interactions between smouldering and flaming of solid wood with the sample and environmental conditions given in the figures.

Figure 3a shows some typical snapshots of StF transition with 60 mm diameter and 20 mm thickness at an airflow velocity of 4.5 m/s. After the airflow was supplied, a smouldering front was propagated into the sample and formed a tiny penetration hole at 429 s. Moreover, the flame was

observed from the side view of the bottom surface at 436 s, and the ignition point could be located at the bottom of the sample, mainly evident by the enveloped flame on the back edge to burnout the sample. This StF transition was in the direction of concurrent smouldering propagation, which is consistent with the observation of Stephen *et al* [26] and Aldushin *et al* [27].

Figure 3b shows that as the sample thickness is decreased to 5 mm, more cracks, even fully penetrated vertical char cracks, have been formed in the heating stage. Under the airflow velocity of 1 m/s, bidirectional glowing combustion was rapidly propagated along the crack, and quickly released much intenser pyrolysis gas than that of Fig. 3a. Smouldering transitioned into flaming eventually, and the small flash first emerged around the small crack at 94 s. The sustained flame dominated the fuel consumption like the phenomena at 160 s.

Further decreasing the airflow velocity, eventually, the StF transition cannot be triggered. Fig. 3c shows some typical photos of the no-transition case, where the forced airflow velocity is 0.5 m/s. Compared to Fig. 3b, similar smouldering ignition and propagation phenomena were observed for the first 20 s, but the glowing propagation rate gradually decreased. As ash covered the surface, the smouldering (glowing) zone became weaker, and almost extinguished at 66 s.

3.2. Characteristics of StF transition

Figure 4 illustrates the IR measurements of the StF transition with a sample thickness of 10 mm at the airflow velocity of 2.5 m/s. After the heating process, two smouldering zones can be indicated by whether or not the oxidizing surface is visible enough to emit brighter glowing light [28–30]. Three points, with points 1-2 in the glowing zone and point 3 in the no-glowing zone on the sample surface near the crack in Fig. 4, were picked to present the temperature distribution of these regions.

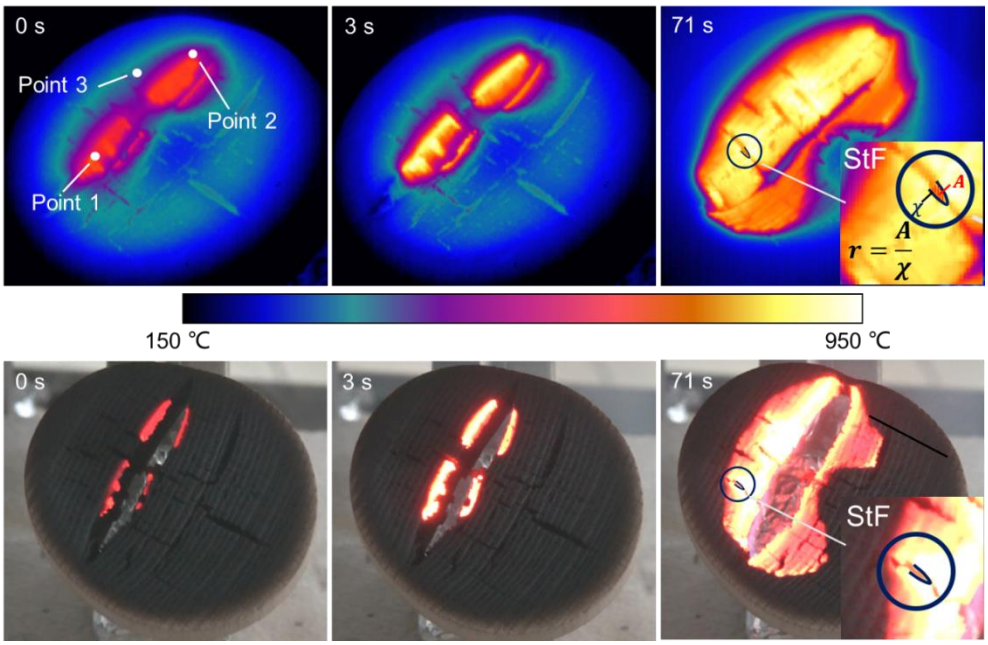

Fig. 4. IR images and snapshots of the top surface around the crack that induced flaming transition of 10 mm thickness sample at 2.5 m/s.

Figure 5a illustrates the temperature profile of points 1-3, around the crack that induced a flaming transition with a sample thickness of 10 mm. At 0 s, the surface temperature was distinguished clearly by the no-glowing smouldering region with low temperature (300-500 °C) and the glowing region with high temperature (600-800 °C) along the crack to the edge. Herein,

(I) a weak and mild smouldering process often has a relatively low surface temperature that is not hot enough to emit visible light, so it is referred to as "(weak) smouldering";

(II) an intensive smouldering surface is hot enough to emit visible red light, so is often referred to as "glowing smouldering".

After an airflow velocity of 2.5 m/s is applied, a similar trend is found for points 1-3. That is, the temperature first increased rapidly and then remained constant over a wide range of time. Subsequently, the temperature slightly increases until the flaming combustion.

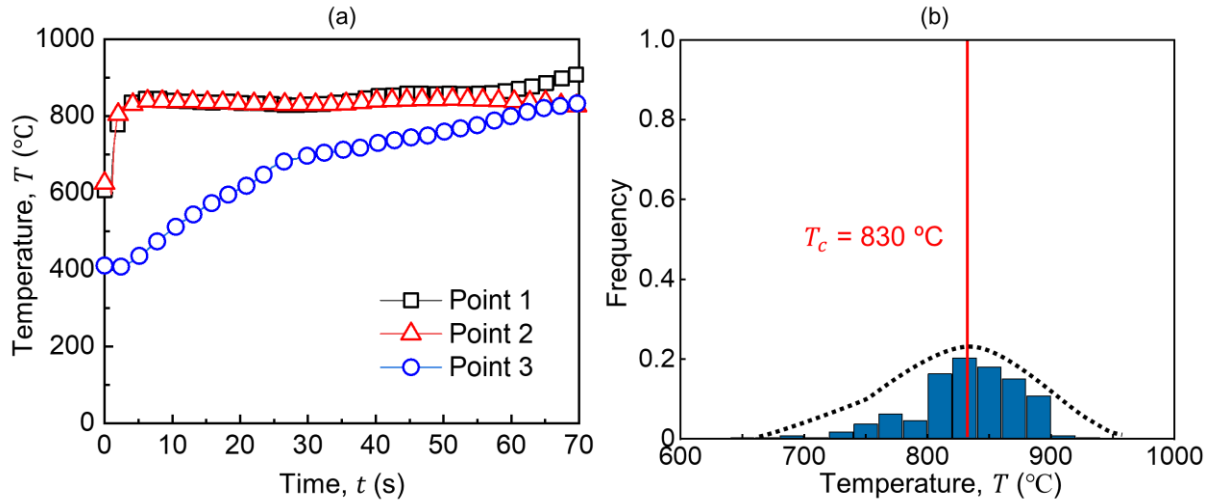

Fig. 5. (a) Temperature evolution at three points of Fig.4, and (b) pixel intensity around the crack that induced flaming transition of 10 mm thickness sample at 2.5 m/s.

Once exposed to the airflow with a duration of 3 s, the temperature of smouldering propagation (point 1) increases from 600 °C to 800 °C, also indicated by the transition from weak smouldering to glowing smouldering. Therefore, the oxygen supply controls the smouldering propagation in this stage. With continuously sustained airflow, the smouldering temperature and propagation rate become stable, and the unlimited oxygen supply no longer affects the smouldering propagation. Instead, the thermal conduction within the fuel should dominate the smouldering propagation. With further accumulated heat, the heat release rate of smouldering or char oxidation may equal or exceed the cooling effect of airflow. Then, the StF transition first occurred near point 1 at 71 s in Fig. 4, wherein the pixel intensity around a radius of 5 mm is presented in Fig. 5b. The average and variance of temperature in this glowing region (T_c) is about 830 ± 30 °C, and is defined as the characteristic temperature of the StF transition. However, for no StF transition case, the highest temperature of the sample surface has been lower than 750 °C. Similar smouldering propagation from the "weak smouldering" transition to the "glowing" state

can be clarified by the time-dependent temperature of point 3 in Fig. 5a.

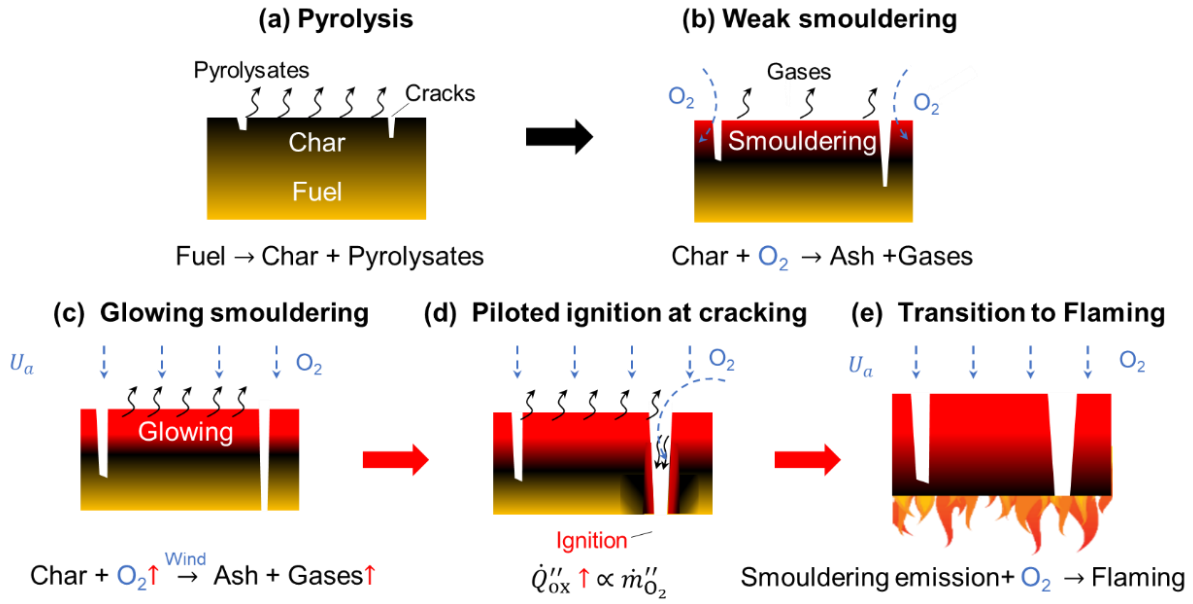

Fig. 6. Schematic diagram of the crack-induced StF (StF) transition of wood.

Figure 6 further explains the processes of crack-induced StF transition under forced convection. In the heating stage, wood first pyrolyzed to form the char and pyrolysates.

$$\text{Wood} \xrightarrow[\text{smouldering}]{\text{heat}} \text{Pyrolysates} + \text{Char (Wood pyrolysis)} \quad (1)$$

On one hand, the temperature difference and thermal expansion in axial and radial directions resulted in the development of thermal stresses. On the other hand, the evaporation of water from wet wood to dry wood and the change of chemical components from drying wood to char would change the mechanical characteristics of the sample as well. These processes were accompanied by shrinkage and cracking in the surface and axial direction against the grain [10,31].

In the force convection stage, smouldering propagation was further preceded by weak smouldering in Fig. 6b and glowing smouldering in 6c, shown as exothermic char oxidation in Eq. 2a.

$$\text{Char} + \text{O}_2 \rightarrow \text{Ash} + \text{CO}_2 + \text{H}_2\text{O (g)} + \text{other gases (Char oxidation)} \quad (2a)$$

The smouldering consumption or shrinkage of the wood material would result in a narrow "burn-through" (penetration) crack. The burn-through region also extended a char zone through the thickness of the wood sample. On one hand, the formation of this narrow vertical channel, an open space to be acted as a "chimney", enhances the air entrainment to the smouldering zone due to the chimney effect. The greater air entrainment increases both the oxygen supply to the smouldering reaction and convective heat losses.

However, the convective heat losses are compensated for by the radiation exchange between the two smouldering surfaces ("U shape") facing each other, which are also more exothermic due to the enhanced air entrainment. Herein, heat irradiation of the two smouldering char surfaces in a vertical

channel can be evaluated as:

$$\dot{q}'' = \varepsilon\sigma(1-F)(T_s^4 - T_0^4) - h(T_s - T_0) \quad (3)$$

where ε is the emissivity of charring, $\sigma = 5.67 \times 10^{-8}\ \mathrm{Wm^{-2}K^{-4}}$ is Stefan–Boltzmann constant, $(1-F)$ is the view factor with which the unit area sees the surroundings, T_s is the temperature of the charring hole and T_0 is the temperature of the pyrolysate mixture. Taking 600 °C and 830 °C surface temperatures of the cracking as an example, the black body radiation will be 32.5 kW/m^2 and 83.5 kW/m^2, respectively, which is nearly triple enhanced to induce the StF transition.

Moreover, the 600 °C and 830 °C surface temperatures respond to 0 and 2.5 m/s airflow, and the heat convection will be about 2.9 kW/m^2 and 16.1 kW/m^2, respectively. Despite the larger airflow increasing the heat convection coefficient, the convective heat losses are compensated for by the radiation exchange between the two smouldering surfaces. Finally, this leads to vigorous smouldering which is favourable for the StF transition. And the origin of the flaming combustion was coincident with the location of the burn-through, and was always first visualised near the bottom of the small penetrating crack. The StF transition can be regarded as the piloted or spontaneous ignition of the pyrolysate-air mixture by the glowing surface of wood, shown in Eq. 2b.

$$\text{Smouldering emissions} + O_2 \xrightarrow{\text{Flame}} CO_2 + H_2O(g)\ \text{(Flaming)} \quad (2b)$$

According to the O_2-based oxygen calorimetry, the HRR of the StF transition can be regarded as the ignition of oxygen and fuel mixture by an enough "hot" glowing surface in Fig. 6d and simplified as

$$\dot{Q}''_{ox} = \Delta H_{O_2} \cdot \dot{m}''_{O_2} \quad (4)$$

where ΔH_{O_2} (J/Kg) is the heat of oxidation, and $\dot{m}''_{O_2}$ (g·m^{-2}·s^{-1}) is the mass flux of oxygen consumption. As airflow velocity increases, the air entrainment and the mixing of fuel and oxygen can be enhanced and accompanied by a higher oxygen supply $\dot{m}''_{O_2}$. This leads to vigorous smouldering which is favourable for the StF transition.

3.3. Airflow effect on StF transition

For the sample thickness of 10 mm, the airflow velocity of 1-6 m/s can lead to a StF transition. Figure 7a illustrates the effect of airflow velocity on the characteristic StF transition temperature (T_c) and delay time that induces the StF transition with this sample thickness. The large error bars of the characteristic temperature (T_c) is attributed to the non-uniform burning of smouldering and StF transition in the area of circles in Fig. 5b and Fig. 7b. As expected, as the airflow velocity increases, the characteristic average temperature increases and the transition time of the StF transition decrease. These trends are agreeing with the theoretical analysis of Eq. 4 where the characteristic average temperature, namely HRR is positively proportional to enhanced airflow, and ignition time is inversely proportional to airflow velocity for constant minimum ignition energy.

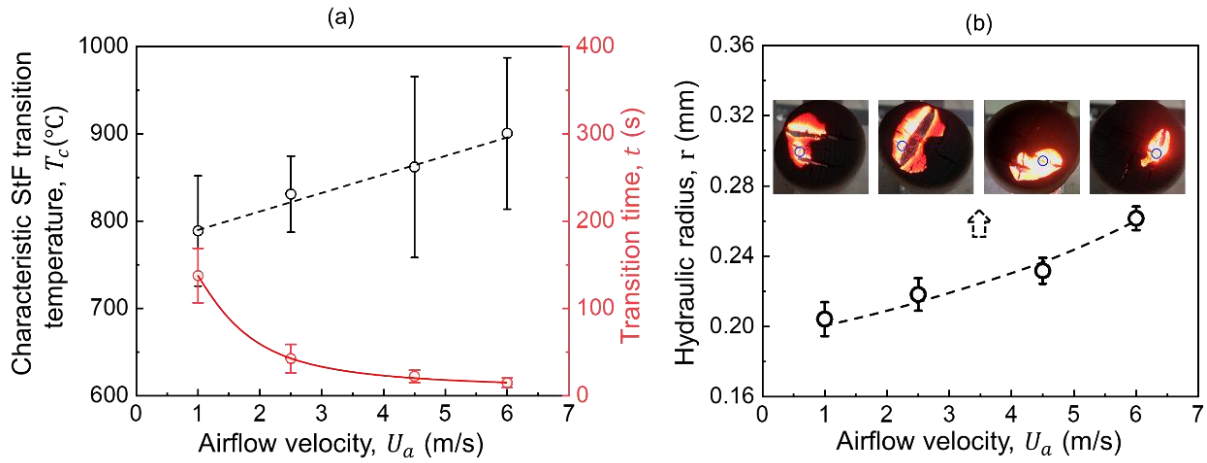

Fig. 7. Effect of airflow velocity on the characteristic StF transition temperature, delay time, and hydraulic radius of smouldering-to-flaming (StF) transition for a 10 mm thick sample.

For example, the characteristic StF transition temperature of the StF transition increases linearly from 788.8°C at 1 m/s to 900 °C at 6 m/s, and the transition delay time decreases from 150 s at 1 m/s to 10 s at 6 m/s. The large error bar of average temperature is attributed to the non-uniform glowing or partially intense glowing as the airflow velocity increases. The asymptote of the transition delay time and airflow (enhanced the glowing surface temperature, analogous to radiation heat flux) in Fig. 7a, seems similar to the relationship of the radiation ignition time and critical heat flux. Note that although not observed in current experiments, in further increasing the external airflow velocity, its cooling effect may become dominant and reduce the risk of a StF transition.

Noticeably, the piloted ignition always occurred by the smallest crack, as a higher concentration of pyrolysates inside the tiny crack. Figure 7b also illustrates the effect of airflow velocity on the hydraulic radius that induces a StF transition with a sample thickness of 10 mm. Here the hydraulic radius (r) is defined as:

$$r = \frac{A}{\chi} \tag{5}$$

where A is the cross-section area, and χ is the corresponding wetted perimeter at the moment of the StF transition, shown in Fig. 4. In general, as the airflow velocity increases, the hydraulic radius increases. For example, the hydraulic radius (r) increases linearly from 0.20 mm at 1 m/s to 0.26 mm at 6 m/s. This was probably because the increased airflow means more exothermic reaction, the critical size like hydraulic radius (r) would increase to resist the enhanced convection cooling.

3.4. Maximum wood thickness and hydraulic radius for StF transition

Figure 8a-b summarizes the experimental results of no StF transition (×), StF transition (●), and transition time under different sample thicknesses. As expected, the maximum wood thickness for the StF transition (δ^*) increases as the thickness of the sample increases. For example, δ^* increases from 10 mm to 40 mm thickness, as the airflow increases from 1 m/s to 6 m/s. There is a rapid growth in δ^* from

10 to 20 mm thickness. For thermally thick wood samples, the thermal penetration depth δ_T [8] at a fixed heating time can be expressed as:

$$\delta_T = \sqrt{12\frac{k}{\rho c}t} \quad (6)$$

here the thermal diffusivity of the specimen is $\frac{k}{\rho c} \approx 5.55\times10^{-8}$ m^2/s, t can be evaluated as the glowing ignition time, which is about 600 s in this experiment. Thus, δ_T is about 20 mm. The pyrolysis depth δ_p [8] is shorter than the heat penetration depth can be estimated as:

$$\delta_p \propto \frac{(T_s - T_p)}{T_s}\sqrt{12\frac{kt}{\rho c}} \quad (7)$$

where T_p and T_s are the pyrolysis and surface temperature of the wood sample, respectively. In this work, δ_p is constant for certain heat flux and heating time, and ranges from 10 to 20 mm. Therefore, only 5 and 10-mm thick samples developed penetrating cracks, which agrees with the experimental phenomena in Fig. 3. Also, there is a rapid growth in δ^* from 10 to 20 mm thickness. Moreover, there is also a rapid growth in the transition time from 10 to 20 mm thickness, such as the transition time is 137 s for 10 mm thickness and 1 m/s wind, and 582 s for 20 mm thickness and 4.5 m/s wind, respectively. This change is because of the limited (or less) thermal penetration depth and the higher structural stiffness as the thickness increases, which also behaves as no penetrating cracks generated for a sample thickness of 20 mm and 40 mm in the heating stage.

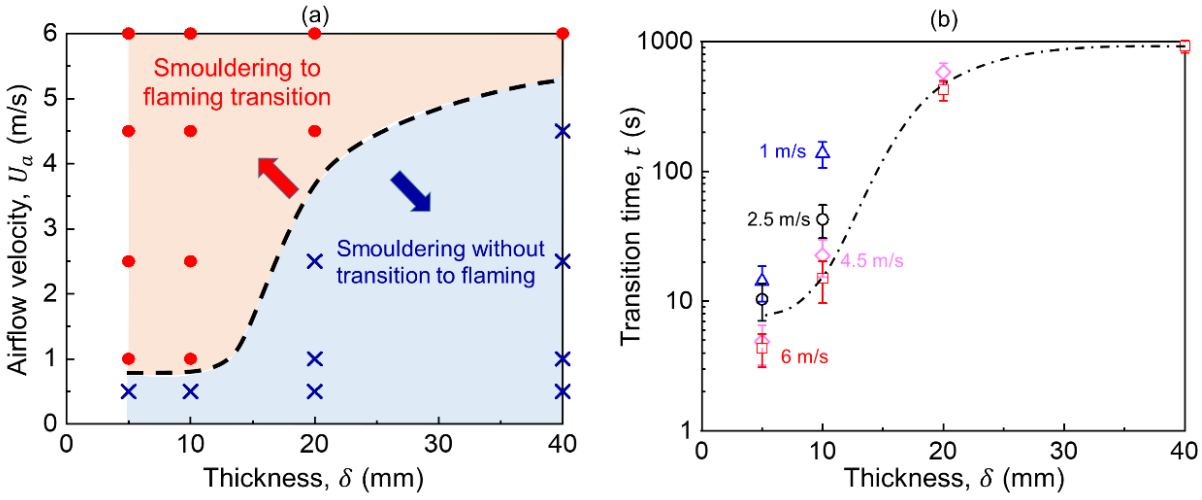

Fig. 8. Effect of sample thickness on (a) experimental outcomes of smouldering or flaming, where no smouldering-to-flaming (StF) transition uses ×, and StF transition uses ●, and (b) delay time of StF transition.

To further explain the influence of airflow velocity and sample thickness on the hydraulic radius (r^*), a simplified energy conservation equation is applied to a propagating smouldering front, as illustrated in Fig. 9a. At the hydraulic radius (r^*), the heat generation in the flaming zone ($\dot{Q}_{fl} = \dot{Q}_{ox}$) due to pyrolysate oxidation being equal to the heat loss to the environment ($\dot{Q}_c$) as

$$\dot{Q}_{fl} = \dot{Q}_{ox} = \dot{Q}_c \quad (8)$$

$$\dot{m}''_{\mathrm{F}}(2\pi r^{*}\delta)\Delta H_F = \dot{m}''_{\mathrm{ox}}(2\pi r^{*}\delta)\Delta H_{\mathrm{ox}} = 2\dot{q}''_{\mathrm{c}}(\pi r^{*2}) \quad (9)$$

$$r^{*} = \frac{\dot{m}''_{\mathrm{F}}\Delta H_F \delta}{\dot{q}''_{\mathrm{c}}} = \frac{\dot{m}''_{\mathrm{ox}}\Delta H_{\mathrm{ox}}\delta}{\dot{q}''_{\mathrm{c}}} \quad (10)$$

where $\dot{m}''_{\mathrm{F}}$ is the flaming burning flux of fuel, ΔH_F is the heat of flaming combustion of fuel which is sensitive to the burning conditions, $\dot{m}''_{\mathrm{ox}}$ is the mass flux of oxygen (i.e., the rate of oxygen supply), ΔH_{ox} is the heat of oxidation, and $\dot{q}''_{\mathrm{c}}$ is cooling flux to the environment. Eq. 10 reveals that the hydraulic radius is proportional to the airflow velocity, which explains the trend of experimental data in Figs. 7b and 9b. But the hydraulic radius is nearly constant with various thicknesses at the given airflow. For example, the hydraulic radius remained nearly 0.26 mm at 6 m/s, and all the hydraulic radii generally remained 0.20-0.27 mm. It is attributed that StF transition is a localized ignition in the gas mixture region. In other words, the effect of the airflow on the hydraulic radius is larger than that of the sample thickness.

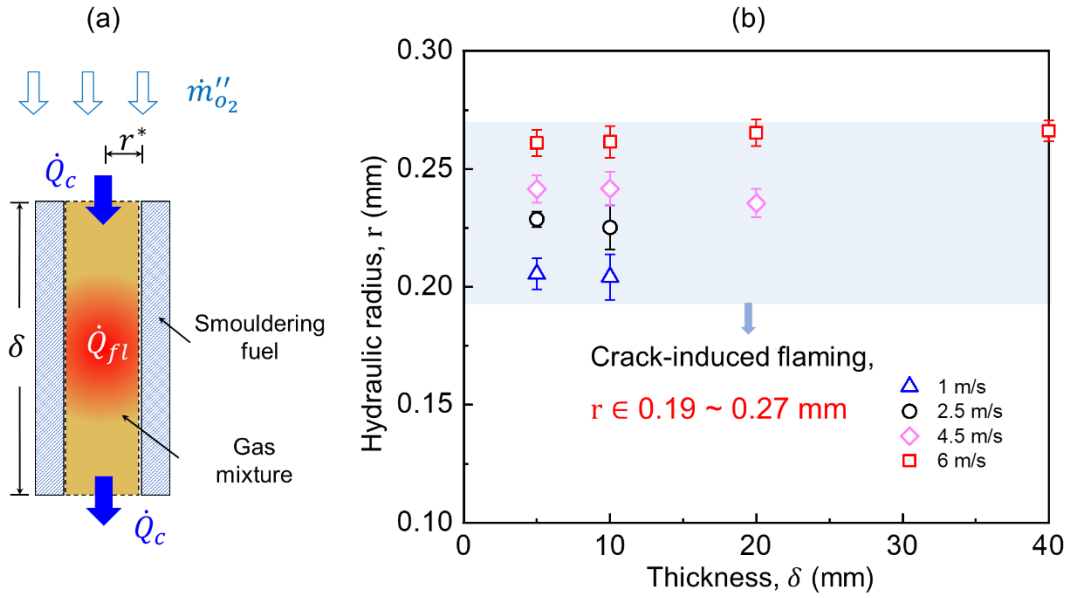

Fig. 9. (a) Schematics for hydraulic radius, and (b) Effect of sample thickness on hydraulic radius.

3.5. Pre-perforated hole effect on StF transition

To verify the effect of penetration crack on the StF transition, Fig. 10 presents the smouldering evolution of a sample thickness of 20 mm with and without a pre-perforated 3 mm-diameter hole at the airflow velocity of 2.5 m/s. As illustrated in Figs. 8a and 10a, this sample without a pre-perforated hole would form several topological char cracks without a "burn-through" penetration. And the glowing region was gradually covered by the ash layer to extinguish the smouldering eventually, which would not induce the StF transition. However, for a pre-perforated case in Fig. 10b, the glowing combustion first emerged near the pre-perforated hole. After the airflow was supplied, the stronger glowing smouldering front was propagated along the pre-perforated hole. Then, the StF transition was successfully induced at the position of this penetration hole from the side view of the bottom surface at

409 s. It implies that the pre-perforated hole, due to the curvature effect, is an alternative shortcut for the smouldering ignition and StF transition, and will reduce the critical airflow of the StF transition from 4.5 to 2.5 m/s. Noticeably, if the size of the pre-perforated hole decreases to a 1 mm diameter, the smouldering front cannot be propagated into the flaming, which is the same as the phenomena without a pre-perforated hole, illustrated in Figs. 8a and 10a.

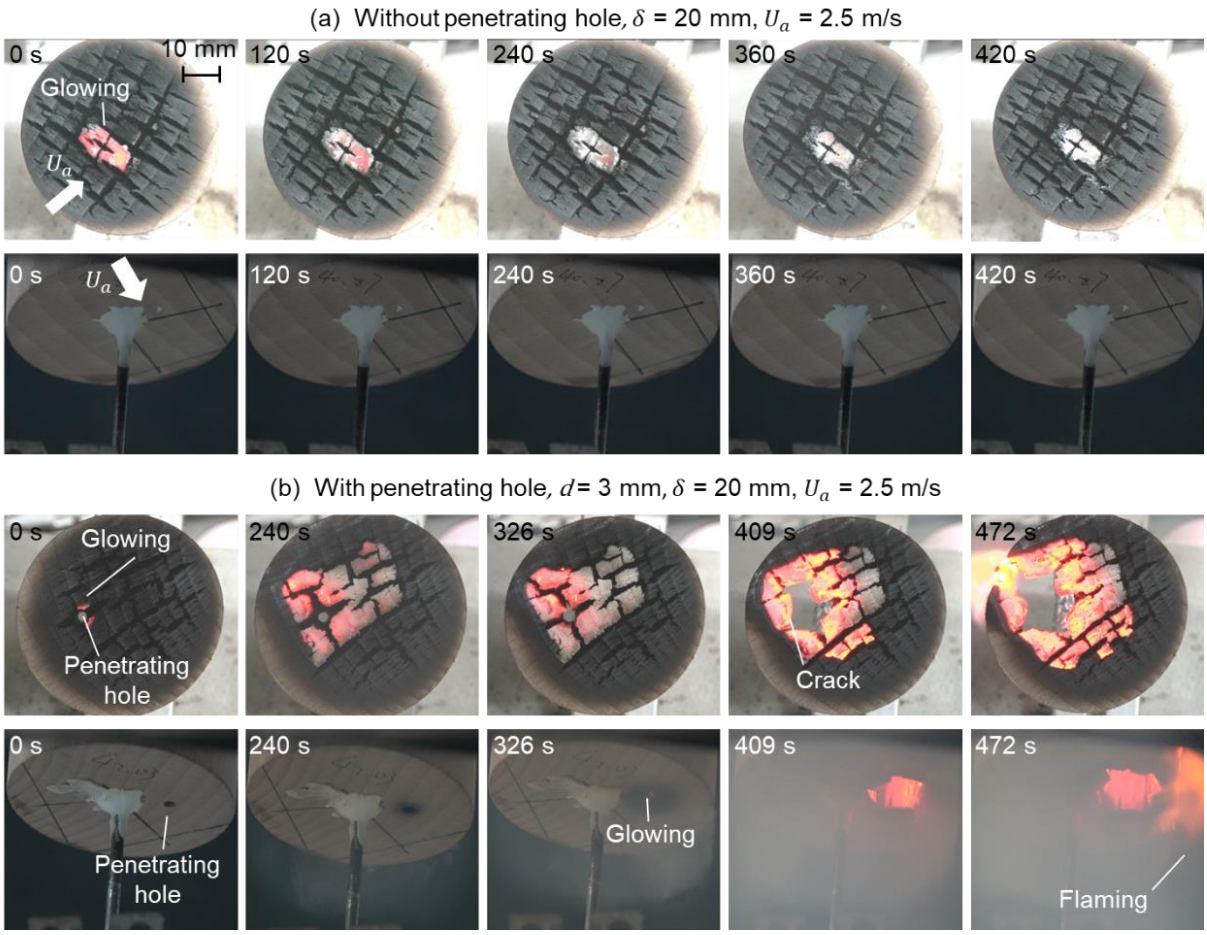

Fig. 10. Evolution of smouldering propagation for (a) self-cracked and (b) pre-perforated sample with a sample thickness of 20 mm at the airflow velocity of 2.5 m/s.

The pre-perforated hole can also verify the effect of airflow direction on the StF transition. The StF transition requires the effective airflow flux to directly pass through the penetrating crack or pre-perforated hole to promote the smouldering propagation [32]. The airflow perpendicular to the smouldering propagation, fails to intensify the oxidation reaction, agreeing with the preliminary experiments that the airflow parallel to the top surface of the sample can not induce the StF transition.

4. Modelling crack-induced StF transition

4.1. Model setup

To further interpret the StF transition and understand the glowing temperature and airflow effect on the transition, a simplified 2-D numerical model is established in Fig. 11. The ignition of the

pyrolysate mixture by the glowing surface in the char cracks, with a δ = 0.01 m vertical high (z) and D^* = 0.001 m horizontal width (x) computational domain, was used to model the StF transition. This horizontal width D^* of the computational domain was evaluated by the average hydraulic diameter, which is four times of hydraulic radius r^*.

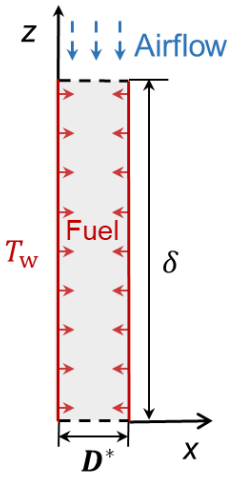

Fig. 11. A scheme of the solution domain of the analytical model.

The produced smouldering emissions were diffused into the reaction zone and mixed with ambient air due to diffusion and forced convection. When the mixture of volatiles and air reaches the lean flammability limit, the oxidation reaction of volatiles induces gas-phase ignition.

In addition, we used the following assumptions and simplifications in modelling:

(1) Heat is transferred from the glowing surface to the gaseous zone by heat conduction and convection.

(2) The combustion of the gas mixture is regarded as laminar flow, and three gaseous concentrations including oxygen (O_2), nitrogen (N_2), and combustible volatiles (gas) are considered. The thermal properties of the gaseous species are temperature independent.

(3) The glowing surface was assumed with a fixed temperature (T_w) boundary, and the smouldering of the solid phase is simplified as a temperature-dependent reactive flow at the boundary and ignored the heat of the char oxidation in the condensed phase.

(4) Ignition occurs when the temperature of the gas mixture undergoes a sharp increase to be much higher than that of the glowing temperature.

(5) Due to the smouldering surfaces in the tiny fissures that are very close to each other, the radiative heat loss through the edge gap into the environment is ignored.

Consistent with the experiments, several cases with various inlet velocities U_a from 0 to 6 m/s at $z = H$ and boundary temperatures T_w ($x = 0$ and $x = L$) from 750 to 1050 °C were modelled. Here T_w is derived from the characteristic StF transition temperature under different wind speeds measured from the IR camera (shown in Fig. 7a). The analytical model outlined above is formulated by the following differential equations.

A global energy equation model is used for volatile combustion, as formulated by

$$\bar{\rho}\bar{c_{\mathrm{p}}}\frac{\partial T}{\partial t}+\bar{\rho}\bar{c_{\mathrm{p}}}(\vec{u}\cdot\nabla)\nabla T=\bar{k}\nabla T+\Delta H_{\mathrm{go}}\rho_{\mathrm{gas}}\left(1-\gamma_{\mathrm{go}}\right)\dot{\omega}_{\mathrm{go}}''' \tag{11}$$

where c_{pi}, ρ_{i}, and k_{i}, ($i=\mathrm{O_2},\mathrm{N_2},\mathrm{gas}$ denoting the oxygen, nitrogen, and combustible volatiles, respectively) are the specific heat, density, and thermal conductivity, respectively. ΔH_{go}, $\dot{\omega}_{\mathrm{go}}'''$, and γ_{go}, heat release, reaction rate and mass stoichiometry of volatiles oxidation. Y_i is the volumetric fraction of species i, and X_i is the mass fraction of species i. The averaged properties in each cell are calculated as

$$\bar{\rho}=\sum Y_i\rho_i,\quad \bar{c_{\mathrm{p}}}=\sum Y_i c_{\mathrm{pi}},\quad \bar{k}=\sum X_i k_i, \tag{12}$$

The momentum equation of oxygen (O_2), nitrogen (N_2) and combustible volatiles (gas) are

$$\bar{\rho}\frac{\partial Y_{\mathrm{O_2}}}{\partial t}+\bar{\rho}(\vec{u}\cdot\nabla)\nabla Y_{\mathrm{O_2}}=\bar{\rho}D\nabla Y_{\mathrm{O_2}}+\rho_{\mathrm{O_2}}\gamma_{\mathrm{o}}\dot{\omega}_{\mathrm{go}}''' \tag{13}$$

$$\bar{\rho}\frac{\partial Y_{\mathrm{N_2}}}{\partial t}+\bar{\rho}(\vec{u}\cdot\nabla)\nabla Y_{\mathrm{N_2}}=\bar{\rho}D\nabla Y_{\mathrm{N_2}} \tag{14}$$

$$\bar{\rho}\frac{\partial Y_{\mathrm{gas}}}{\partial t}+\bar{\rho}(\vec{u}\cdot\nabla)\nabla Y_{\mathrm{gas}}=\bar{\rho}D\nabla Y_{\mathrm{gas}}+\rho_{\mathrm{gas}}((1-\gamma_{\mathrm{c}})\dot{\omega}_{\mathrm{py}}'''-\gamma_o\dot{\omega}_{\mathrm{go}}''') \tag{15}$$

respectively. Where D is the diffusion coefficient of the decomposed gases. For simplification, all gaseous species are assumed the same diffusivity $D=2\times10^{-5}\ \mathrm{m^2/s}$.

The mass conservation and laminar flow (compressible flow Ma < 0.3) equations of the gas mixture are as follows:

$$\bar{\rho}\nabla\vec{u}=0 \tag{16}$$

$$\bar{\rho}\frac{\partial\vec{u}}{\partial t}+\bar{\rho}(\vec{u}\cdot\nabla)\vec{u}=-\nabla p+\nabla\mu(\nabla\vec{u}+(\nabla\vec{u})^T) \tag{17}$$

The initial conditions are

$$\vec{u}=0,\ p=0; \tag{18}$$

$$Y_{\mathrm{O_2}}=0.21, Y_{\mathrm{N_2}}=0.79, Y_{\mathrm{gas}}=0; \tag{19}$$

$$T=293.15\ \mathrm{K},\ T|_{x=0\&L}=T_{\mathrm{w}}; \tag{20}$$

The boundary conditions are:

1. The left and right surfaces are set as the no-slip wall. The upper and bottom surfaces are the inlet and outlet surfaces, respectively.

$$\vec{u}|_{x=0}=0 \tag{21}$$

$$\vec{u}|_{x=L}=U_a \tag{22}$$

$$(-\nabla p+\mu(\nabla\vec{u}+(\nabla\vec{u})^T)|_{z=0\&H}=0 \tag{23}$$

2. Combustible volatiles are generated from the no-slip wall and the mass transfer with the external on open boundaries.

$$-\rho_{\mathrm{O_2}}D\frac{\partial Y_{\mathrm{O_2}}}{\partial z}|_{z=0\&H}=h_{\mathrm{m}}(Y_{\mathrm{O_2}}^{\infty}-Y_{\mathrm{O_2}}|_{z=0\&H}) \tag{24}$$

$$-\rho_{\mathrm{N_2}}D\frac{\partial Y_{\mathrm{N_2}}}{\partial z}|_{z=0\&H}=h_{\mathrm{m}}(Y_{\mathrm{N_2}}^{\infty}-Y_{\mathrm{N_2}}|_{z=0\&H}) \tag{25}$$

$$-\rho_{\mathrm{gas}}D\frac{\partial Y_{\mathrm{gas}}}{\partial z}|_{z=0\&H}=h_{\mathrm{m}}(Y_{\mathrm{gas}}^{\infty}-Y_{\mathrm{gas}}|_{z=0\&H}) \tag{26}$$

$$-\rho_{\mathrm{gas}}D\frac{\partial Y_{\mathrm{gas}}}{\partial x}|_{x=0\&L}=\dot{\omega}_{\mathrm{py}}'''\rho_{\mathrm{gas}}H \tag{27}$$

here h_m is the mass transfer coefficient obtained from [33,34].

3. The temperature of the no-slip wall is the characteristic value of the StF transition (T_w) measured in the experiment.

$$T|_{z=0\&H} = 293.15\ \text{K} \tag{28}$$

$$T|_{x=0\&L} = T_w \tag{29}$$

Eqs. (11-17) are solved by finite element methods, using the GMRES (Generalized Minimal Residual) iteration method. The steady-state solution is computed for simplification, which is sufficient to resolve the calculations. And the domains are divided into 0.1 mm × 0.1 mm meshes. When the mesh size decreases by a factor of 2, the numerical results vary less than 0.5%, so the grid resolution is well solved.

4.2. Effect of boundary temperature on StF transition

To illustrate the effect of boundary temperature on the StF transition, the temperature and density of the gaseous reaction are presented in Fig. 12a, with 780, 800 and 820 °C boundary temperatures with an airflow velocity of 2.5 m/s. As the boundary temperature increased, the concentration of gaseous combustion increased to the maximum value of 820 °C boundary temperature. With the characteristic temperature of the StF transition at 830 °C (obtained from the experiment), only boundary temperatures of 800 and 820 °C can induce the ignition of a pyrolysate-oxygen mixture.

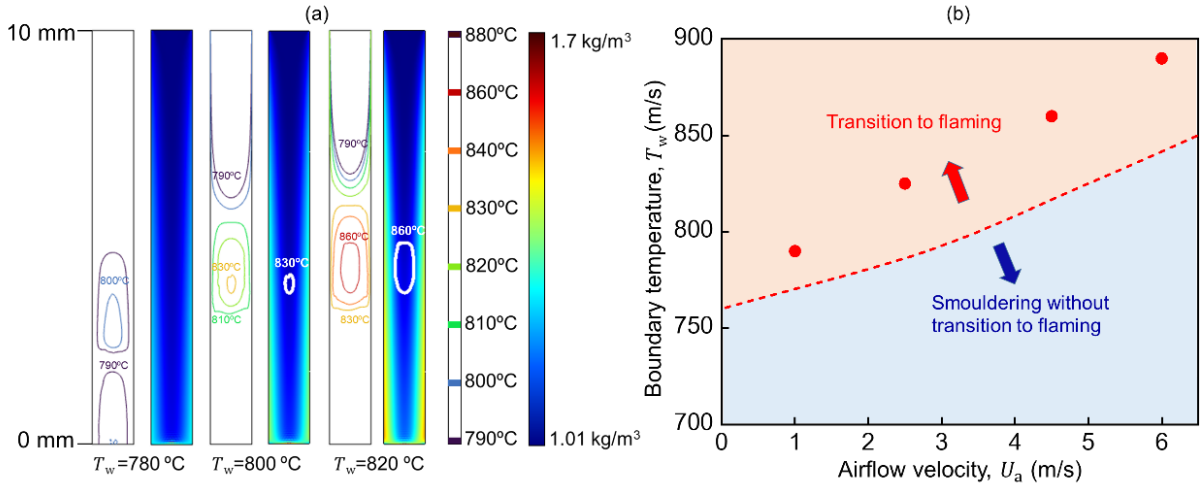

Fig. 12. (a) Temperature and density of gaseous with T_w = 780, 800 and 820 °C at the airflow velocity of 2.5 m/s, and (b) two regimes of smouldering-to-flaming (StF) transition and critical line by the numerical model, and the scatter of experimental data are also presented.

Therefore, the critical glowing surface temperature can be summarized as the two ignition regimes in Fig. 12b. The critical glowing surface temperature increases as the airflow velocity increases, agreeing with the experimental results in Fig. 7a. The differences in critical glowing surface temperature between the experimental results and numerical model, are attributed that the char oxidation or the radiative heat loss have been neglected in the model. The extrapolation of the minimum boundary temperature to the StF transition has also been obtained in the model, even without external airflow.

This temperature value is approximately 760 °C, and difficult to achieve for the smouldering combustion of wood in no wind condition.

4.3. Effect of airflow on StF transition

Figure 13 illustrates the airflow effect on the temperature field and the related ignition point at T_w= 800 °C with the airflow velocity of 1 m/s, 2.5 m/s, 4 m/s and 6 m/s. The ignition first occurred at the highest temperature of the gas mixture, which would be located in the centre of the char crack, away from the glowing surface. Thus, it inferred that the transition of StF seems to be the auto-ignition of a pyrolysate-oxygen mixture, and is induced by the heat transfer from hot smouldering surfaces.

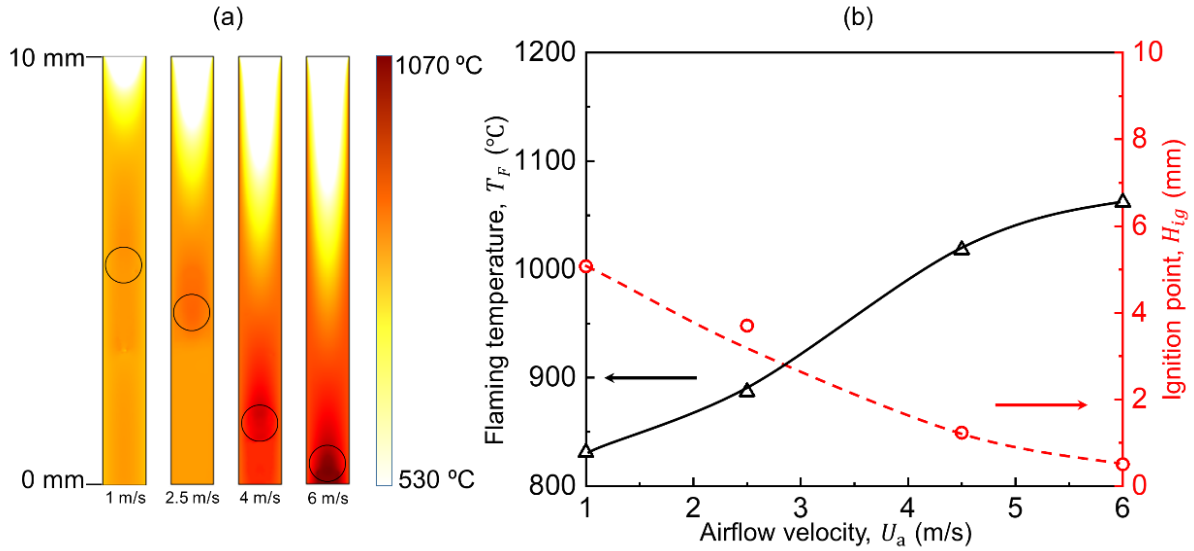

Fig. 13. Temperature distribution and the related ignition point for various airflow velocities at T_w= 800 °C.

As airflow velocity increases, the higher flaming temperature illustrates more intensive gas-phase homogenous oxidation to compensate for the convective heat loss due to the airflow, agreeing with the experimental results in Fig. 7a. Therefore, oxygen supply controls the smouldering propagation in this regime, while the cooling effect of airflow is negligible. Moreover, more air and pyrolysates are entrained into the internal region of the hole. This results in the ignition point moving down to the bottom gradually, as shown in Fig. 13b.

4.4. Effect of chimney configuration on StF transition

In literature, experiments on chimneys are always with different shapes, i.e., square, rectangular, and slot-shaped [7]. Herein, for simplification, the crack was assumed as a rectangle in former models. As illustrated in Fig. 3, the crack is nearly an inverted trapezoid in the cross-section, which is modelled as well to test the shape effect on the model results. Here the trapezoid, with a top base of 0.001 m, a bottom base of 0.0008 m, and a height of 0.01 m, has an area of 0.000009 m², nearly the same as the area of a rectangle (0.00001 m²).

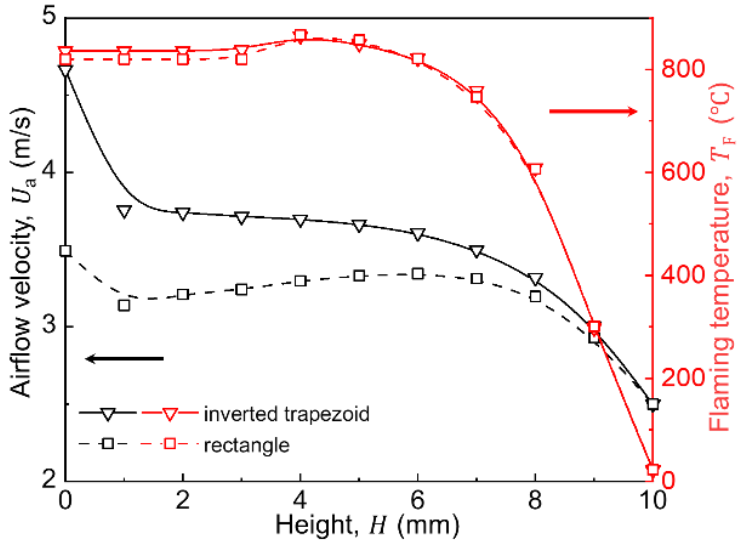

Fig. 14. Airflow velocity and temperature in the centre of the char crack of the inverted trapezoid and rectangle crack with a typical case (U_a = 2.5 m/s and T_w = 800°C)

Comparison of the airflow velocity and temperature between the inverted trapezoid and rectangle crack with a typical case (U_a = 2.5 m/s and T_w = 800 °C) illustrates in Fig. 14. The airflow velocity of the inverted trapezoid crack is larger than that of the rectangle crack, and the difference increases along the direction of airflow. However, the rectangle or inverted trapezoid cracks have a negligible effect on the critical boundary temperature and the ignition point that induces the StF transition. It also proves the rationality of rectangle crack in turn.

5. Conclusions

In this work, a series of experiments were performed to investigate the smouldering and flaming burning behaviour of solid wood, and the StF transition limit with a diameter of 60 mm and thicknesses of 5-40 mm under external airflows up to 6 m/s. Results show that the smouldering-to-flaming (StF) transition can be observed under external airflow at about 830 °C under external airflow, which is caused by the interaction between smouldering-induced crack and environmental airflow. Herin, the weak and glowing smouldering can be measured as low temperature (300-500 °C) and high temperature (600-800 °C), respectively.

The fully penetrated vertical char crack or pre-perforated hole promotes the StF transition because of (1) enhanced radiation between the two smouldering surfaces and (2) greater air supply under the chimney effect. As the wind velocity ($\dot{m}''_{O_2}$) increases, both the smouldering surface temperature ($\dot{Q}''_{ox}$) and crack size increase, so the delay time of the StF transition becomes shorter. For a larger wood thickness, a larger airflow is required to generate the crack and cause a StF transition. But the hydraulic radius generally remained 0.20-0.27 mm with various thicknesses at the given airflow.

A numerical model is proposed to investigate the volatile convection and flaming ignition. Numerical analysis reproduces the StF transition, as an autoignition of a pyrolysate-oxygen mixture

promoted by hot smouldering surfaces. The numerical model further reveals the effects of smouldering temperature and cross wind on the StF transition. This work deepens the understanding of the StF transition dynamics and provides insights into the wildfire ignition dynamics and fire hazards of timber structures.

Declaration of Competing Interest

None.

Acknowledgements

This work is sponsored by the National Natural Science Foundation of China (52176113), Shanghai Sailing Program (22YF1452400), and University Natural Science Research Project in Jiangsu Province (21KJA620003).

Credit author statement

Ziyang Zhang: Investigation, Writing - Original Draft, Formal analysis.

Pengfei Ding: Investigation, Writing - Original Draft, Formal analysis.

Supan Wang: Conceptualization, Investigation, Methodology, Writing - Original Draft, Formal analysis; Funding acquisition.

Xinyan Huang: Methodology, Formal analysis; Supervision, Writing - Review & Editing.

References

[1] J. Song, C. Chen, S. Zhu, M. Zhu, J. Dai, U. Ray, Y. Li, Y. Kuang, Y. Li, N. Quispe, Y. Yao, A. Gong, U.H. Leiste, H.A. Bruck, J.Y. Zhu, A. Vellore, H. Li, M.L. Minus, Z. Jia, A. Martini, T. Li, L. Hu, Processing bulk natural wood into a high-performance structural material, Nature. 554 (2018) 224–228. https://doi.org/10.1038/nature25476.

[2] C. Chen, Y. Kuang, S. Zhu, I. Burgert, T. Keplinger, A. Gong, T. Li, L. Berglund, S.J. Eichhorn, L. Hu, Structure–property–function relationships of natural and engineered wood, Nat. Rev. Mater. (2020) 19–21. https://doi.org/10.1038/s41578-020-0195-z.

[3] J.G. Quintiere, Fundamentals of Fire Phenomena, 2006. https://doi.org/10.1002/0470091150.

[4] R. Emberley, A. Inghelbrecht, Z. Yu, J.L. Torero, Self-extinction of timber, Proc. Combust. Inst. 36 (2017) 3055–3062. https://doi.org/10.1016/j.proci.2016.07.077.

[5] S. Mcallister, M. Finney, Autoignition of wood under combined convective and radiative heating, Proc. Combust. Inst. 36 (2017) 3073–3080. https://doi.org/10.1016/j.proci.2016.06.110.

[6] N. Liu, J. Lei, W. Gao, H. Chen, X. Xie, Combustion dynamics of large-scale wildfires, Proc. Combust. Inst. 38 (2021) 157–198. https://doi.org/10.1016/j.proci.2020.11.006.

[7] T. Ohlemiller, Smoldering Combustion Propagation On Solid Wood, Fire Saf. Sci. 3 (1991) 565–574. https://doi.org/10.3801/iafss.fss.3-565.

[8] K. Li, S. Hostikka, P. Dai, Y. Li, H. Zhang, J. Ji, Charring shrinkage and cracking of fir during pyrolysis in an inert atmosphere and at different ambient pressures, Proc. Combust. Inst. 36

(2017) 3185–3194. https://doi.org/10.1016/j.proci.2016.07.001.

[9] K. Li, Y. Zou, S. Bourbigot, J. Ji, X. Chen, Pressure effects on morphology of isotropic char layer, shrinkage, cracking and reduced heat transfer of wooden material, Proc. Combust. Inst. (2020). https://doi.org/10.1016/j.proci.2020.07.072.

[10] S. Wang, P. Ding, S. Lin, X. Huang, A. Usmani, Deformation of wood slice in fire: Interactions between heterogeneous chemistry and thermomechanical stress, Proc. Combust. Inst. 38 (2021) 5081–5090. https://doi.org/10.1016/j.proci.2020.08.060.

[11] S. Wang, P. Ding, S. Lin, J. Gong, X. Huang, Smoldering and Flaming of Disc Wood Particles Under External Radiation: Autoignition and Size Effect, Front. Mech. Eng. 7 (2021) 1–11. https://doi.org/10.3389/fmech.2021.686638.

[12] S. Lin, T.H. Chow, X. Huang, Smoldering propagation and blow-off on consolidated fuel under external airflow, Combust. Flame. 234 (2021) 111685. https://doi.org/10.1016/j.combustflame.2021.111685.

[13] M.A. Santoso, E.G. Christensen, J. Yang, G. Rein, Review of the Transition From Smouldering to Flaming Combustion in Wildfires, Front. Mech. Eng. (2019). https://doi.org/10.3389/fmech.2019.00049.

[14] Y. Chen, Z. Liang, S. Lin, X. Huang, Limits of sustaining a flame above smoldering woody biomass, Combust. Sci. Technol. (2022). https://doi.org/10.1080/00102202.2022.2041000.

[15] K.N. Palmer, Smouldering combustion in dusts and fibrous materials, Combust. Flame. 1 (1957) 129–154. https://doi.org/10.1016/0010-2180(57)90041-X.

[16] A. Bar-Ilan, O.M. Putzeys, G. Rein, A.C. Fernandez-Pello, D.L. Urban, Transition from forward smoldering to flaming in small polyurethane foam samples, Proc. Combust. Inst. 30 (2005) 2295–2302. https://doi.org/10.1016/j.proci.2004.08.233.

[17] A.B. Dodd, C. Lautenberger, C. Fernandez-Pello, Computational modeling of smolder combustion and spontaneous transition to flaming, Combust. Flame. 159 (2012) 448–461. https://doi.org/10.1016/j.combustflame.2011.06.004.

[18] S.I. Stoliarov, O. Zeller, A.B. Morgan, S. Levchik, An experimental setup for observation of smoldering-to-flaming transition on flexible foam/fabric assemblies, Fire Mater. 42 (2018) 128–133. https://doi.org/10.1002/fam.2464.

[19] S. Lin, X. Huang, J. Gao, J. Ji, Extinction of Wood Fire: A Near-Limit Blue Flame Above Hot Smoldering Surface, Fire Technol. (2021). https://doi.org/10.1007/s10694-021-01146-6.

[20] M.A. Finney, J.D. Cohen, J.M. Forthofer, S.S. McAllister, M.J. Gollner, D.J. Gorham, K. Saito, N.K. Akafuah, B.A. Adam, J.D. English, R.E. Dickinson, Role of buoyant flame dynamics in wildfire spread, Proc. Natl. Acad. Sci. U. S. A. 112 (2015) 9833–9838. https://doi.org/10.1073/pnas.1504498112.

[21] G. Rein, Smoldering Combustion, in: SFPE Handb. Fire Prot. Eng., Springer New York, New York, NY, 2014: pp. 581–603. https://doi.org/10.1007/978-1-4939-2565-0_19.

[22] T.J. Ohlemiller, Forced smolder propagation and the transition to flaming in cellulosic insulation, Combust. Flame. 81 (1990) 354–365. https://doi.org/10.1016/0010-2180(90)90031-L.

[23] J. Yang, N. Liu, H. Chen, W. Gao, Smoldering and spontaneous transition to flaming over horizontal cellulosic insulation, Proc. Combust. Inst. 37 (2019) 4073–4081.

https://doi.org/10.1016/j.proci.2018.05.054.

[24] J. Gong, M. Zhang, Y. Jiang, C. Zhai, Z. Wang, Limiting condition for auto-ignition of finite thick PMMA in forced convective airflow, Int. J. Therm. Sci. 161 (2021) 106741. https://doi.org/10.1016/j.ijthermalsci.2020.106741.

[25] S. Lin, X. Huang, J. Gao, J. Ji, Extinction of Wood Fire: A Near-Limit Blue Flame Above Hot Smoldering Surface, Fire Technol. 58 (2022) 415–434. https://doi.org/10.1007/s10694-021-01146-6.

[26] S.D. Tse, A. Carlo, F. Nde-Pello, K. Miyasaka, Controlling mechanisms in the transition from smoldering to flaming of flexible polyurethane foam, Symp. Combust. 26 (1996) 1505–1513. https://doi.org/10.1016/S0082-0784(96)80372-9.

[27] A.P. Aldushin, A. Bayliss, B.J. Matkowsky, Is there a transition to flaming in reverse smolder waves?, Combust. Flame. 156 (2009) 2231–2251. https://doi.org/10.1016/j.combustflame.2009.09.009.

[28] N. Boonmee, J.G. Quintiere, Glowing ignition of wood: The onset of surface combustion, Proc. Combust. Inst. 30 (2005) 2303–2310. https://doi.org/10.1016/j.proci.2004.07.022.

[29] C.L. Beyler, Ignition Handbook, Fire Science Publishers/Society of Fire Protection Engineers, Issaquah, WA, 2004. https://doi.org/10.1023/b:fire.0000026981.83829.a5.

[30] J. Yang, A. Hamins, L. Dubrulle, M. Zammarano, Experimental and computational study of glowing ignition of wood, Fire Mater. (2021) 1–13. https://doi.org/10.1002/fam.3089.

[31] D. Baroudi, A. Ferrantelli, K.Y. Li, S. Hostikka, A thermomechanical explanation for the topology of crack patterns observed on the surface of charred wood and particle fibreboard, Combust. Flame. 182 (2017) 206–215. https://doi.org/10.1016/j.combustflame.2017.04.017.

[32] R.A. Ogle, J.L. Schumacher, Fire Patterns on Upholstered Furniture: Smoldering versus Flaming Combustion, Fire Technol. 34 (1998) 247–265.

[33] M.A.B. Zanoni, J.L. Torero, J.I. Gerhard, Determining the conditions that lead to self-sustained smouldering combustion by means of numerical modelling, Proc. Combust. Inst. 37 (2019) 4043–4051. https://doi.org/10.1016/j.proci.2018.07.108.

[34] S. Lin, H. Yuan, X. Huang, A computational study on the quenching and near-limit propagation of smoldering combustion, Combust. Flame. 238 (2022) 111937. https://doi.org/10.1016/j.combustflame.2021.111937.

[35] S. Wang, H. Chen, N. Liu, Ignition of expandable polystyrene foam by a hot particle: An experimental and numerical study, J. Hazard. Mater. 283 (2015) 536–543. https://doi.org/10.1016/j.jhazmat.2014.09.033.

Appendix:

The chemical reaction in the StF process can be described by a simplified 2-step global kinetics

$$\text{Fuel} \rightarrow \gamma_{\text{py}}\text{Char} + (1-\gamma_{\text{py}})\text{Pyrolysis Gas} \quad \text{(A1)}$$

$$(1-\gamma_{\text{go}})\text{Pyrolysis Gas} + \gamma_{\text{go}} O_2 \rightarrow \text{Products} \quad \text{(A2)}$$

where γ is the mass stoichiometric coefficient and $\gamma_{\text{py}} = \rho_{char}/\rho_{fuel}$, $\gamma_{\text{go}} = \rho_{O_2}/\rho_{mix}$. The reaction rate of the 2-step global kinetic scheme is expressed using Arrhenius law as

$$\dot{\omega}_{\text{k}}''' = A \cdot \exp(-\frac{E}{RT}) \quad \text{(A3)}$$

The formation and decomposed rate of combustible volatiles are $(1-\gamma_{\text{py}}) \cdot \dot{\omega}_{\text{py}}'''$ and $(1-\gamma_{\text{go}}) \cdot \dot{\omega}_{\text{go}}'''$, respectively. The corresponding heat of the gaseous reaction is $(1-\gamma_{\text{go}}) \cdot \dot{\omega}_{\text{go}}''' \cdot \rho_{\text{gas}} \cdot \Delta H_{\text{go}}$. The reaction parameters of the 2-step reaction are obtained from [23,35], listed in Table.1.

Table.1. Reaction parameters of the 2-step reaction

Parameter	Pyrolysis	Flame
A (s^{-1})	4.58×10^{7}	3.5×10^{8}
E (kJ/mol)	160	160
ΔH (MJ/kg)	-0.533	55

Physical properties of all gaseous species are also obtained from [23,35] or measured in this study and listed in Table.2. The averaged properties of a gas mixture are calculated by weighting volume fractions of all species as

$$k_{mix} = \sum Y_i \cdot k_i, M_{mix} = \sum Y_i \cdot M_i, c_{p,mix} = \sum Y_i \cdot c_{p,i}, \rho_{mix} = \sum Y_i \cdot \rho_i \quad \text{(A4)}$$

where the subscripts i represent the number of gas-phase species.

Table.2. The physical parameters of condensed-phase species

Species	k (W/m-K)	ρ (kg/m^3)	c_p (J/kg-K)	M (g/mol)
Oxygen (O_2)	0.0240	1.141	920	32
Nitrogen (N_2)	0.0228	1.25	1.038	28
Volatiles (Gas)	0.0258	2.1	840	44